Natural Resources for Human Health
eISSN: 2583-1194

Original Research

Received 20 May 2026
Revised 29 June 2026
Accepted 26 July 2026

Natural Resources for Human Health 2026, Vol. 6 (8s): 786–809

KEYWORDS:
Trussless roofing; cold-formed steel; roof-to-beam connection; wind load; seismic load; IS 875; IS 1893; finite element analysis; response surface methodology

Wind- and Seismic-Zone-Calibrated Selection of Roof-to-Beam Base Connections for Long-Span Trussless Roofing Systems: A Mechanics-Based Framework for Indian Design Practice

[1]*Surya Prakash, [2]Dr. Sachin Balkrishna Mulay

[1]PhD Research Scholar, Sandip University, Department of Civil Engineering, School of Engineering & Technology, Sandip University, Nashik, Maharashtra – 422213, India
[2]Associate Dean, Sandip University, Department of Civil Engineering, School of Engineering & Technology, Sandip University, Nashik, Maharashtra – 422213, India
[1]spsingh.jmd@gmail.com and [2]sachin.mulay@sandipuniversity.edu.in
[1]ORCID: 0009-0006-4886-095X and [2]ORCID: 0000-0002-8281-0183

ABSTRACT:

Introduction: Trussless (self-supported) roofing systems built from curved, cold-formed Galvalume steel sheets have become a default long-span roofing solution for Indian warehouses, logistics parks, and industrial sheds, yet Indian design practice still lacks codified guidance for the roof-to-support base connection through which the entire wind-uplift and seismic reaction of the arched roof is transferred to the substructure. Validated finite-element and response-surface studies have compared candidate base-connection types, but their loading envelopes are expressed in generic pressure and acceleration units that are not referenced to the wind and seismic zone maps used in Indian design, IS 875 (Part 3):2015 and IS 1893 (Part 1):2016. Practicing engineers are consequently left without a direct, code-referenced basis for selecting a base-connection type for a given Indian site.

Methods: Four field-constructible roof-to-beam base connections — traditional mechanical anchor, cap plate, support bracket, and continuous steel frame — were evaluated under identical wind-uplift and seismic loading using coupled shell-contact finite element analysis (ANSYS Mechanical; SHELL181 shell elements; Coulomb-friction surface contact; multipoint-constraint bolt formulations) together with a two-factor response surface methodology (RSM) design (Design-Expert v13). The analysed loading envelope (wind pressure 1.0–2.0 kN/m²; seismic acceleration 0.10–0.25g) was explicitly mapped, using the IS 875 (Part 3):2015 design wind pressure equation and the IS 1893 (Part 1):2016 zone-factor table, onto the basic wind speed range (33–55 m/s) and seismic zones (II–V) that govern Indian construction.

Results: Peak von Mises stress at the base connection fell by 60.1% and mid-span deflection by 20.0% moving from the traditional anchor to the continuous frame, while per-bolt load demand was halved. ANOVA confirmed wind pressure as the sole statistically significant driver of vertical response ($p < 0.0001$), with no measurable seismic contribution across the tested envelope ($p = 1.0000$). Mapping the tested wind-pressure range against IS 875 (Part 3):2015 shows that it corresponds to basic wind speeds of approximately 43–61 m/s for eave heights of 10 m or more — spanning India's high-wind-speed and cyclone-exposed zones — while the tested seismic range (0.10–0.25g) covers IS 1893 (Part 1):2016 Zones II through just above Zone IV, leaving

Zone V (Z = 0.36) outside the validated envelope.

Discussion: For Indian sites with basic wind speeds at or above approximately 44–47 m/s — much of the eastern and western coastline and the cyclone belt — the traditional bolted anchor develops base stresses and per-bolt demands large enough to make the cap plate, bracket, or continuous frame the mechanically justified choice; the continuous frame is recommended without qualification wherever wind speed, redundancy, or maintenance access is design-critical. The seismic-insignificance finding holds for Zones II–IV but should not be extrapolated to Zone V without further validation.

Conclusion: This zone-calibrated framework provides Indian design engineers with connection-selection guidance for trussless roofing systems that is, for the first time, directly referenced to IS 875 and IS 1893 provisions rather than to generic laboratory load ranges.

1. INTRODUCTION

Self-supported, or trussless, roofs were first developed for small industrial buildings with spans of up to about 20 m (Nikam & Joshilkar, 2016) and have since become widespread because of their low cost, rapid installation, and curved, seam-free appearance (Singh et al., 2024). Rapid growth of the Indian warehousing, e-commerce, and logistics sectors has made the system a default choice for long-span industrial roofing, because it shortens construction schedules and accelerates return on investment for owners and developers. Curved standing-seam panels are roll-formed and crimp-curved from flat coil using mobile, on-site equipment, then joined by cold seaming before being lifted onto pre-positioned supports (Dharsono & Gilang, 2023); the resulting jointless surface reduces both leak paths and long-term maintenance.

Structurally, the curved sheet acts as a two-hinged arch, transferring load principally through compression to the supporting structure, and must be checked against both wind (Pannachet & Karasudhi, 2013) and seismic (Horsakulthai & Wichit, 2013) demands. The mechanics of the arched sheet itself — buckling behaviour, load-bearing capacity, and stress distribution in profiled or corrugated steel arch roofs — has been investigated analytically, experimentally, and numerically for two decades (S. M. Zahurul Islam et al., 2005; Wu et al., 2006; Narvydas & Puodžiuniene, 2013; Piekarczuk et al., 2015; Sumathi & Divya, 2022; Zhdanov & Ulasevich, 2016; Guerrero-Cuasapaz et al., 2021; Piekarczuk et al., 2021). What these studies share is a focus on the roof sheet as a shell or arch element; comparatively little attention has been paid to the roof-to-beam base connection, the single interface through which the arch thrust, wind uplift, seismic inertia, rotation, sliding, and construction tolerance must all be resolved simultaneously.

A companion investigation by the present authors addressed the member-level design gap directly, deriving wind and seismic loads for a representative Indian trussless-roof building under IS 875 (Part 3):2015 and IS 1893 (Part 1):2016 and validating the resulting arch, column, and continuous-beam sections in STAAD Pro against an independent cold-formed-steel design tool (RSG-CFS) (Prakash & Mulay, unpublished manuscript). That study, consistent with earlier reviews of the technology (Nikam & Joshilkar, 2016; Singh et al., 2024), reiterated that Indian codes provide no explicit design methodology for trussless roofing and that, in its absence, commercial fabricators frequently under-design for wind and seismic demand. It modelled the roof-to-beam interface, however, as an idealised pinned support released against moment transfer, and did not examine the connection hardware — anchors, plates, brackets, or frames — that must physically realise that support in the field.

A separate and more recent body of research has examined connection-level behaviour in wind-loaded metal roofing in considerable depth. A state-of-the-art review confirmed that damage in wind-loaded metal roof cladding typically initiates at local connection details rather than through uniform sheet yielding (Tiwari et al., 2025). Full-scale testing of standing-seam roofs has shown that 27–46% of applied wind load can redistribute to eaves and gables before clip disengagement (Xia et al., 2023); equivalent-spring and pullout-failure models have been developed for high-vertical standing-seam clip connections (Yang et al., 2024; Liang, Yang, Liu, Nie, et al., 2024; Liang, Yang, Liu, & Wang, 2025); bearing-capacity formulae have been derived for standing-seam systems from 281 finite element models (Chen et al., 2024); and sliding supports, screw-fastened claddings, and welded L-shaped supports have each been characterised experimentally and numerically (Table 1). These studies converge on the same conclusion — that connection stiffness and detailing, not sheet material strength, govern roof performance under wind — but every one of them addresses a purlin-supported, seam-clip, or screw-fastened interface. None examines the discrete roof-to-RCC-beam base connection that is specific to trussless arched roofs, and none expresses its loading envelope with reference to a national wind or seismic zone map, so the results, while mechanically rigorous, cannot be translated directly into a connection choice for a specific Indian site.

The present authors previously undertook a direct comparison of four field-constructible base-connection types for a 20 m trussless arch — traditional mechanical anchor, cap plate, support bracket, and continuous steel frame — using coupled finite-element and response-surface methods, and found that increasing contact continuity and area, rather than sheet strength, controlled the stress-strain state of the connection (Prakash & Mulay, unpublished manuscript-b). That comparison, like the wider connection literature it responded to, specified its wind-pressure and seismic-acceleration inputs as generic laboratory ranges (1.0–2.0 kN/m^2 and 0.10–0.25g respectively) rather than as values referenced to IS 875 (Part 3):2015 or IS 1893 (Part 1):2016. Left unresolved, this creates exactly the condition that motivated the companion member-level study: a validated result that a practicing engineer in India cannot use directly, because it is not stated in terms the applicable design codes recognise.

The objective of the present study is therefore to re-examine that finite-element/response-surface comparison of the four base-connection systems specifically to (i) derive, from first principles, the design wind pressure and seismic zone-factor relationships prescribed by IS 875 (Part 3):2015 and IS 1893 (Part 1):2016; (ii) map the previously analysed loading envelope onto these code provisions to establish which Indian wind and seismic zones the validated results do and do not cover; and (iii) translate the combined mechanical and code-mapping findings into connection-selection guidance that can be applied directly against the Indian wind-speed and seismic-zone maps, thereby closing — at the connection level — the same codal gap previously identified at the member level for trussless roofing in India.

Table 1. Summary of experimental, numerical, and analytical studies on wind-loaded metal roof connections and cladding systems

Reference	Objective	Methodology	Materials / Parameters	Key Finding	Relevance
Wu et al. (2020)	Explain uplift failure stages	Quasi-dynamic tests, FE simulation	Standing seam roof system	Three-stage failure mechanism identified	Supports staged connection assessment
Sun et al. (2021)	Quantify wind vulnerability	Numerical reliability analysis	Damage index, performance levels	Multistage vulnerability curves derived	Links damage states to design criteria
Min et al. (2021)	Improve sliding support capacity	Testing and numerical analysis	Sliding support, tensile strength	Sliding displacement 2.0–3.24× higher	Shows support-geometry importance
Lu et al. (2022)	Reinforce seam-locked roofs	Detailed FE modelling	Sliding support, sandwich panel	Bearing capacity 3.24× baseline	Shows connection-strengthening effect
Roy (2023a)	Test interlocking cladding uplift	Pressure tests, nonlinear FE	Thickness, yield stress, span	Screw-region failure at connections	Confirms fastener-localised damage

Roy (2023b)	Test weatherboard uplift capacity	24 tests, 264 FE models	0.48–0.55 mm CFS claddings	Local clip failure near tek screws	Confirms connection-zone weakness
Pieper & Mahendran (2023)	Model corrugated cladding pull-through	Validated Abaqus parametric study	Geometry, thickness, washer, span	Plastic dimpling at screw holes	Supports bolt-hole stress focus
Darwish & ElGawady (2023)	Model retrofitted metal roofs	High-fidelity FE validation	TPO membrane, fastener spacing	Uplift deformation field captured	Supports validated roof FE modelling
Jiang et al. (2024)	Assess welded roof support fatigue	Tensile fatigue experiments	SUS304 L-shaped supports	Safe cyclic-load range established	Supports cyclic connection durability
Cheng & Cheng (2024)	Compare roofing wind resistance	Wind uplift tests, FE simulation	Al-Mg-Mn, stainless-steel systems	Continuous welded system 25%+ stronger	Supports continuous-connection advantage

2. MATERIALS AND METHODS

2.1 Material Preparation

Trussless roofing panels were fabricated from AZ150 Galvalume steel coils comprising 55% aluminium, 43.5% zinc, and 1.5% silicon by mass, coated to ASTM A792 Grade D at a nominal coating mass of 150 g/m² (AZ150/AZ200 designation). The coils exhibited a yield strength of 350–550 MPa, an elastic modulus of 200 GPa, and an elongation at fracture of 20–25%. Galvalume was selected in preference to conventional galvanised steel for its superior atmospheric corrosion resistance and self-healing behaviour under minor coating abrasion, particularly relevant under the coastal and industrial exposure typical of Indian warehouse siting. The mechanical and geometric properties of all structural components used across the four connection systems are listed in Table 2; the composition figures are consistent with those independently reported for the same material grade in the companion member-level design study (Prakash & Mulay, unpublished manuscript), providing a cross-check on the material characterisation.

Table 2. Material properties of structural components used in trussless-roof base-connection construction

Component	Grade / Type	Yield Strength (MPa)	Elastic Modulus (GPa)	Elongation (%)	Surface Treatment
Galvalume steel sheet	AZ150, 0.8 mm (ASTM A792 D)	350–550	200	20–25	Al-Zn-Si coating, 150 g/m²
Anchor bolts	M16, Fe 410	240	200	22	Galvanised / zinc coated
RCC beam	M25 concrete	25 (compressive)	30	—	Surface ground finish
Cap plate	Fe 410, 6 mm	250	200	23	Red oxide primer + paint

Natural Resources for
Human Health
eISSN: 2583-1194

Support bracket	SHS 72 × 72 × 4 mm	250	200	20	Epoxy coated
Frame angle	ISA 50 × 50 × 6 mm	250	200	21	Epoxy coated

2.2 Panel Manufacturing and Erection

Panels 600 mm wide were produced on a portable hydraulic roll-forming (MIC) machine fed from flat Galvalume coil: a cold-pressing die first forms a trapezoidal corrugation with a 75 mm rib pitch and 25 mm rib height along the coil, after which a press cutter trims each panel to length (Figure 1). The panel is then passed through a second portable hydraulic machine for crimp-curving, which imparts the design arch radius in discrete increments so that the finished panel meets both structural and aesthetic requirements. The curved profile transfers load principally through two-hinged arch action (Figure 2), so that the roof-to-support base connection must resist the resulting horizontal thrust in addition to vertical uplift and any seismic inertial demand — the specific structural problem addressed in this study.

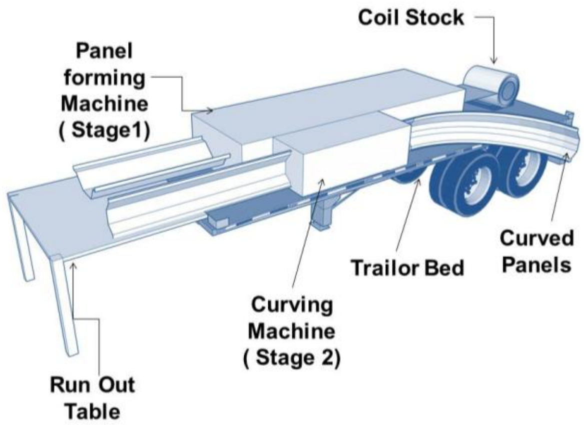

Figure 1. On-site roll-forming and crimp-curving of curved roofing panels.

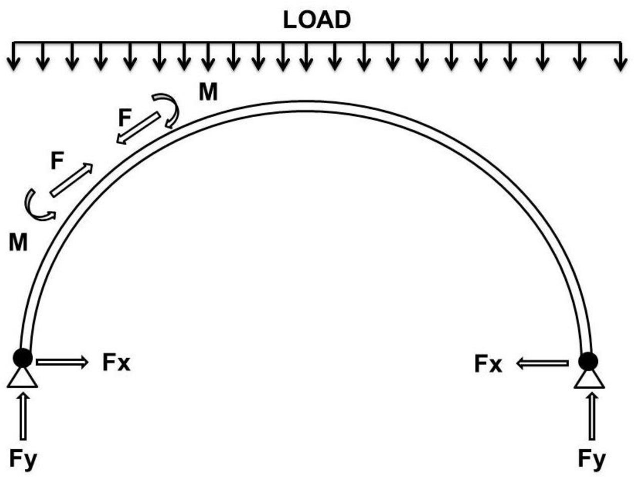

Figure 2. Two-hinged arch mechanics governing load transfer in the trussless roof sheet.

Three curved panels are joined by seam-locking at ground level before erection, using a mechanical seaming device that closes the standing seam without holes, bolts, overlaps, or sealants; this ground-level assembly improves quality control and removes the safety hazard of seaming at height. The seamed triplet is then lifted by crane onto pre-positioned column supports and mechanically anchored to a continuous supporting member — of reinforced concrete or structural steel — that must itself be proportioned to resist the lateral thrust generated by the arch (Figure 3). It is this continuous member, and specifically its interface with the curved sheet, that is the subject of the present connection comparison. For the connection FE study reported here, a 20 m arch span was used; this is comparable to the 18 m span, 8 m rise example building (Pune, India; basic wind speed 39 m/s; Seismic Zone III) used in the companion member-level study to illustrate code-based load derivation, and both fall within the 15–25 m span range typical of Indian trussless warehouse construction, so the connection-selection guidance developed here is expected to remain applicable across that range.

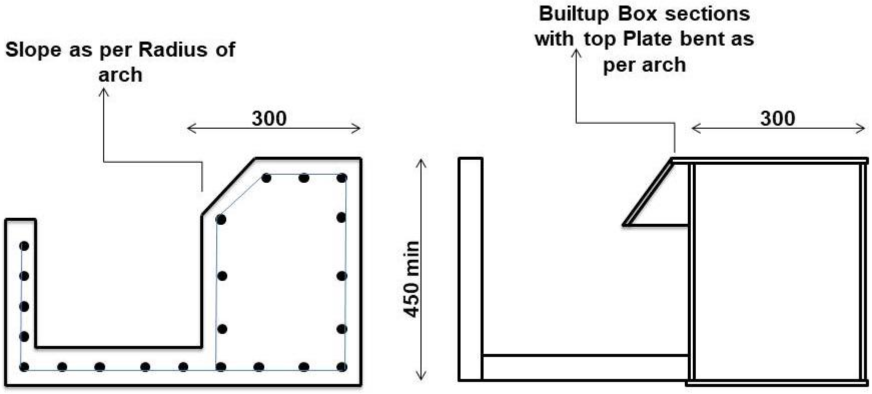

Figure 3. Continuous RCC or steel support beam receiving the trussless roof panel; the roof-to-beam interface at this member is the subject of the present comparison.

2.3 Base Connection Configurations

Four base-connection systems were constructed for comparative evaluation under identical material, loading, and environmental conditions; their engineering detailing is shown in Figure 4, and the corresponding effective contact-interface areas in Figure 5. The traditional anchor system used M16 chemical anchor bolts drilled through the corrugated sheet into the M25 RCC beam at 5 bolts per metre, providing a discrete contact area of 0.2 m² per metre. The cap plate system used a 150 × 150 × 6 mm Fe 410 plate over the sheet at the beam interface, secured by M16 bolts at 6 per metre, extending the effective contact area to 0.4 m² per metre. The support bracket system comprised an SHS 72 × 72 × 4 mm inclined bracket anchored to a 175 × 175 × 6 mm base plate with 300 mm M16 bolts at 8 per metre, achieving 0.7 m² per metre. The continuous steel frame used an ISA 50 × 50 × 6 mm angle running continuously along the RCC beam, fastened at 10 bolts per metre, providing an uninterrupted 1.0 m² per metre of contact.

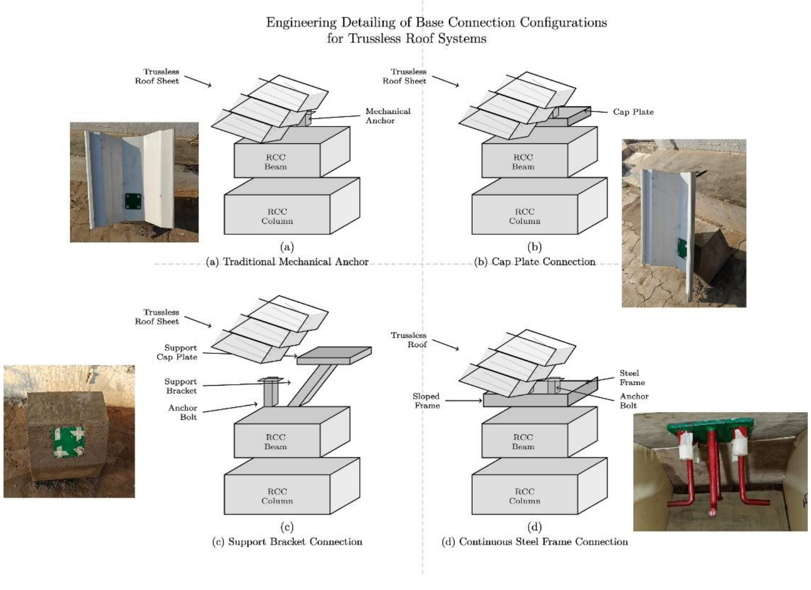

Figure 4. Engineering detailing of the four base connection configurations: (a) traditional anchor, (b) cap plate, (c) support bracket, (d) continuous steel frame. Source: authors.

Natural Resources for
Human Health
eISSN: 2583-1194

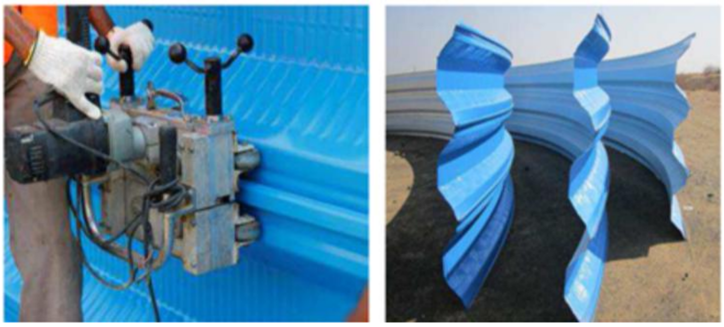

Figure 5. Effective contact interface area for each configuration, increasing progressively from 0.2 m²/m (traditional anchor) to 1.0 m²/m (continuous frame).

2.4 Test Setup and Instrumentation

All specimens were tested at 25 ± 2 °C and 55 ± 5% relative humidity, with pre-curved panel assemblies seated on M25 RCC beam supports replicating field boundary conditions (Figure 6). Wind pressure was applied as a uniformly distributed load normal to the upper panel surface using a purpose-built hydraulic pressure frame, incremented from 0.50 to 2.00 kN/m² in steps of 0.25 kN/m², with each increment held for 60 seconds before gauge reading. Vertical mid-span deflection was measured using 0.01 mm-resolution dial gauges on a rigid reference frame independent of the specimen, and contact stress intensity at the base interface was recorded using FLA-5-11 foil strain gauges (Tokyo Sokki Kenkyujo Co., Japan) bonded to the connection steel at the beam contact zone, with data acquired at each load increment after stabilisation.

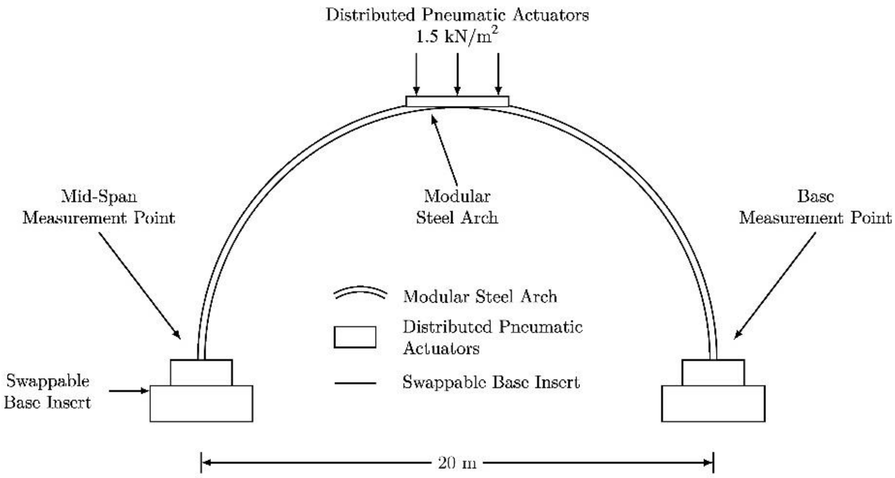

Figure 6. Schematic of the experimental setup. Source: authors.

2.5 Numerical Modelling

Parametric finite element models of each connection configuration were built in SolidWorks 2023 (Dassault Systèmes, France) and analysed in ANSYS Mechanical 2023 R1 (ANSYS Inc., USA) as spatial (three-dimensional) shell-contact models rather than plane-stress or plane-strain idealisations, so that curvature and torsional effects were retained (Table 3, Figure 7). The corrugated panel was discretised explicitly using SHELL181 four-node reduced-integration shell elements, with the 75 mm/25 mm rib geometry modelled along the full 600 mm panel width without homogenisation, preserving the anisotropic flexural stiffness of the corrugated section. Symmetry boundary conditions on the lateral edges represented continuity with adjacent seam-locked units, and fixed translational restraints were applied at all RCC beam support nodes.

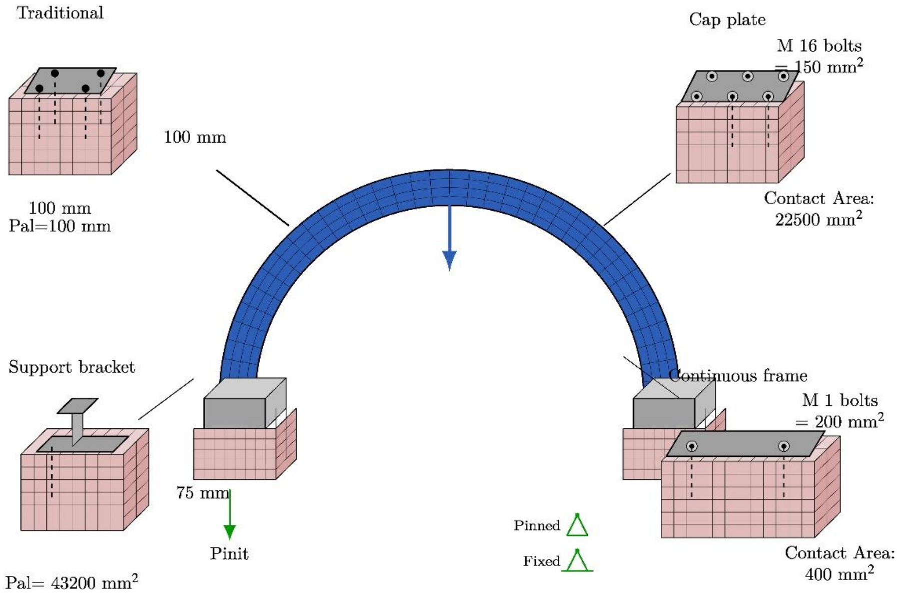

Figure 7. Parametric finite element model in ANSYS. Source: authors.

Surface-to-surface contact pairs at all connection interfaces used a Coulomb friction model, with μ = 0.3 at steel-to-steel interfaces and μ = 0.45 at steel-to-concrete interfaces; normal behaviour was hard contact, permitting separation under uplift. Bolt shanks were modelled as beam elements coupled to the surrounding shell mesh through multipoint-constraint (MPC) equations. The material was treated as linear elastic, consistent with a service-level stress-strain assessment rather than an ultimate-limit-state study (Table 3). Wind pressure was applied as a uniform surface load normal to the curved panel over q_a = 1.0–2.0 kN/m² (reference case 1.5 kN/m²), and seismic action was introduced as horizontal base excitation at the support level with peak ground acceleration ađ = 0.10–0.25g (Figure 8). Vertical response was quantified as mid-span deflection, δ_{mix}, and stress response as base stress intensity, σ^b, at the roof-to-beam interface.

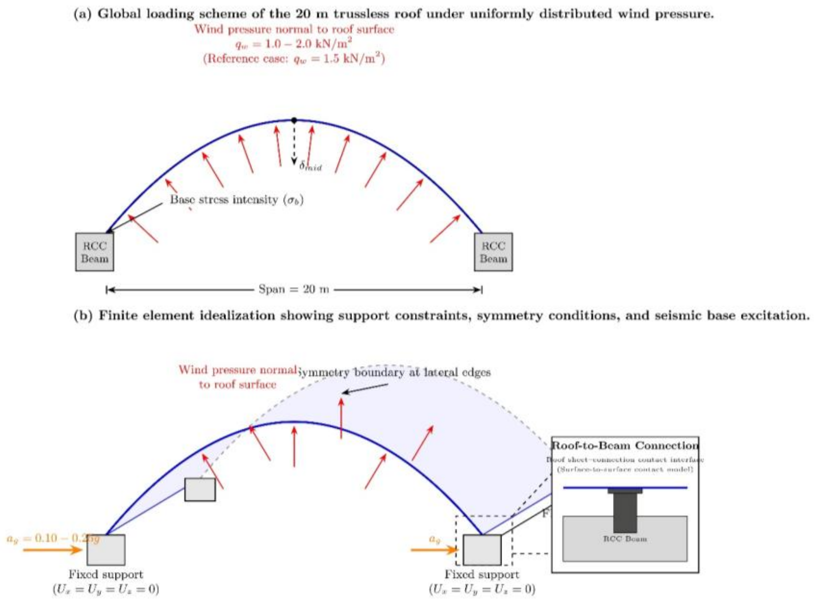

Figure 8. Loading and boundary conditions for the trussless roof model: (a) arch under wind pressure normal to the surface; (b) FE idealisation with fixed RCC supports, lateral symmetry, seismic base excitation, and roof-to-beam contact interface.

Table 3. Numerical idealisation and constitutive assumptions used in the finite element model.

Modelling item	Adopted setting	Implication
Problem formulation	Spatial finite element model	3D shell-contact response represented
Plane assumption	Not plane stress / strain	Curvature and torsion retained
Roof panel	SHELL181 curved shell	Corrugation stiffness preserved
Model width	600 mm strip	Adjacent panels represented by symmetry
Lateral boundaries	Symmetry constraints	Seam-locked continuity simulated
Support condition	Fixed RCC support nodes	Base translations restrained
Wind loading	Normal surface pressure	Curved shell loading represented
Seismic loading	Horizontal base excitation	Support-level inertial action applied
Contact behaviour	Hard contact with friction	Separation under uplift permitted
Bolt modelling	Beam elements with MPC	Bolt-sheet coupling represented
Material model	Linear elastic	Service-level stress-strain response assessed
Plasticity	Not activated	Yielding not modelled

2.6 Mesh Sensitivity Study

Three mesh refinement levels — coarse (15 mm, 4,820 elements), medium (8 mm, 18,640 elements), and fine (4 mm, 71,250 elements) — were evaluated at a reference wind pressure of 1.5 kN/m², with convergence set at less than 2% variation between successive levels for both responses (Table 4). The variation between medium and fine meshes was below 2% for both deflection and stress, so the medium mesh (8 mm, 18,640 elements) was adopted for all subsequent analyses.

Table 4. Mesh sensitivity results for mid-span deflection and base stress intensity under 1.5 kN/m² wind pressure.

Mesh level	Element size (mm)	Elements	Deflection (mm)	Stress (kN/m²)	Deflection variation (%)	Stress variation (%)
Coarse	15	4,820	9.21	12.10	—	—
Medium	8	18,640	8.07	10.08	12.4	16.7
Fine	4	71,250	8.00	10.00	0.87	0.79

2.7 Validation Protocol

FEA-predicted mid-span deflection was compared against experimentally measured values at each of seven load increments (0.50–2.00 kN/m²) for all four connection configurations, giving 28 internal validation points, with percentage deviation calculated as $|\text{FEA} - \text{Experimental}| / \text{Experimental} \times 100$. FEA predictions were additionally cross-validated against independently published experimental results for mid-span deflection range, peak connection stress, deflection reduction ratio, and seismic contribution.

2.8 Statistical Analysis (Response Surface Methodology)

A two-factor response surface methodology (RSM) design was implemented in Design-Expert v13 (Stat-Ease Inc., USA) to quantify the effects of wind pressure (Factor A: 1.0–2.0 kN/m²) and seismic acceleration (Factor B: 0.10–0.25g) on mid-span deflection and base stress intensity, using a full two-factor linear design with centre-point replication (13 runs). Linear regression models fitted to the FEA response data gave the following predictive equations in coded factor form:

Mid-span deflection (mm) = 8.00 + 2.67A + 0.0000B   (1)

Base stress intensity (kN/m²) = 10.00 + 3.33A + 0.0000B   (2)

where A is the coded wind-pressure value and B the coded seismic-acceleration value. Model adequacy was assessed by ANOVA, the coefficient of determination (R^2), and the Adequate Precision ratio.

2.9 Correlating the Analysis Envelope with IS 875 (Part 3):2015 and IS 1893 (Part 1):2016

The finite element and RSM analysis above, like the connection and cladding literature it builds on (Table 1), specifies its loading envelope in generic pressure and acceleration units. To make the results usable against Indian design codes, the tested envelope was mapped onto the design wind pressure equation of IS 875 (Part 3):2015 and the zone-factor table of IS 1893 (Part 1):2016, using the same coefficients and simplifying assumptions (terrain category 2; $k_1 = k_3 = k_4 = 1.0$) adopted for the representative Indian trussless-roof building in the companion member-level study (Prakash & Mulay, unpublished manuscript).

IS 875 (Part 3):2015 defines the design wind speed as $V_r = V^b \cdot k_1 \cdot k_2 \cdot k_3 \cdot k_4$, where V^b is the basic wind speed; the design wind pressure is then $p_r = 0.6V_r^2$ (N/m²), reduced by a further factor of 0.8 for structures with eave height below 10 m (Clause 6.3, Note), and finally combined with the directionality, area-averaging, and combination factors ($k^d \cdot k_a \cdot k^c = 1 \times 1 \times 0.9 = 0.9$ for the roof zone considered) to give the design wind pressure p^d. Applying this relationship across the basic wind speeds that appear on the IS 875 wind zone map of India (V^b = 33–55 m/s) gives the design pressures in Table 5.

Table 5. Design wind pressure (IS 875 Part 3:2015) across the Indian basic wind speed range, for low-rise (eave height < 10 m) and taller (≥ 10 m) trussless-roof buildings.

Basic wind speed, V^b (m/s)	p_x (kN/m²)	p^d, eave height < 10 m (kN/m²)	p^d, eave height ≥ 10 m (kN/m²)
33 (e.g., much of central/peninsular India)	0.653	0.470	0.588
39 (e.g., Pune/Nashik region — companion study site)	0.913	0.657	0.821
44	1.162	0.836	1.045
47 (moderate cyclone exposure)	1.325	0.954	1.193
50 (high cyclone exposure)	1.500	1.080	1.350
55 (highest zone — e.g., parts of the Odisha, West Bengal, and Gujarat coast)	1.815	1.307	1.633

Solving the same relationship for p^d = 1.0 and 2.0 kN/m² — the lower and upper bounds of the FEA/RSM envelope — gives $V^b \approx 48$ m/s (low-rise) or ≈ 43 m/s (eave height ≥ 10 m) at the lower bound, and $V^b \approx 68$ m/s (low-rise) or ≈ 61 m/s (eave height ≥ 10 m) at the upper bound. Because the highest basic wind speed on the current IS 875 map is 55 m/s, the tested envelope brackets the entire range of Indian wind zones for buildings of 10 m eave height or more (design pressure at V^b = 55 m/s is 1.63 kN/m², within the tested range), and covers the upper wind-speed zones ($V^b \gtrsim$ 44–47 m/s) even for low-rise sheds; it does not extend down to the design pressures applicable to low-rise buildings in the lowest wind-speed zones ($V^b \approx$ 33–39 m/s, p^d = 0.47–0.66 kN/m²), for which the present results should be read as an upper-bound, conservative estimate of connection demand rather than an interpolated one (Section 3.8).

IS 1893 (Part 1):2016 assigns each of the four seismic zones a zone factor, Z, representing the effective peak ground acceleration expected under the maximum considered earthquake: Z = 0.10 for Zone II, 0.16 for Zone III, 0.24 for Zone IV, and 0.36 for Zone V (Table 6). The tested seismic-acceleration range in the FEA/RSM design, 0.10–0.25g, therefore corresponds almost exactly to Zones II through III and extends just beyond the Zone IV factor, but falls well short of the Zone V factor of 0.36g — a gap of 44% beyond the upper tested value.

Table 6. IS 1893 (Part 1):2016 seismic zone factors and their coverage by the tested FEA/RSM envelope.

Seismic zone	Zone factor, Z (g)	General hazard level	Covered by tested envelope (0.10–0.25g)?
II	0.10	Low (much of peninsular India)	Yes — lower bound
III	0.16	Moderate (e.g., Nashik/Pune region)	Yes
IV	0.24	High (Indo-Gangetic belt, NCR, parts of Bihar and J&K)	Yes — just within upper bound
V	0.36	Very high (Kashmir valley, Kachchh, Northeast India, Andaman & Nicobar)	No — 44% beyond upper bound

3. RESULTS

3.1 Mid-Span Deflection Under Wind Loading

Figure 9 presents mid-span deflection for the four connection systems under the reference wind pressure of 1.5 kN/m². The traditional anchor recorded the highest deflection, 10.0 mm. The cap plate reduced this to 9.0 mm (10.0% reduction), the support bracket to 8.5 mm (15.0% reduction), and the continuous steel frame to the lowest value, 8.0 mm (20.0% reduction relative to the traditional anchor). The total response range across all four systems was 8.0–10.0 mm.

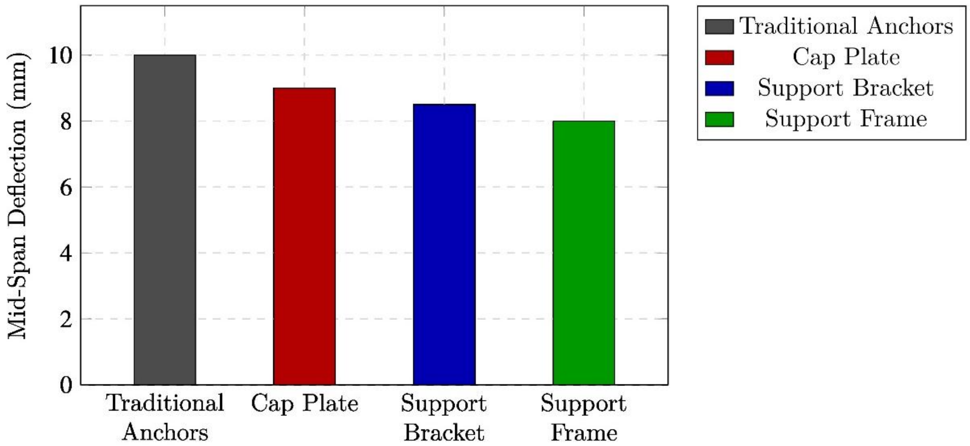

Figure 9. Comparative mid-span deflection of trussless-roof base connections under uniform wind pressure of 1.5 kN/m².

3.2 Base Stress Intensity and Load Distribution

Figure 10 shows the stress intensity at the arch base for each system under a simulated vertical load of 10 kN per metre length. The traditional anchor produced the highest base stress, 50.0 kN/m², over a contact area of 0.2 m². The cap plate reduced this to 25.0 kN/m² (50.0% reduction) over 0.4 m²; the support bracket to 14.3 kN/m² (71.4% reduction) over 0.7 m²; and the continuous steel frame to the lowest value, 10.0 kN/m² (80.0% reduction), over the full 1.0 m² contact surface.

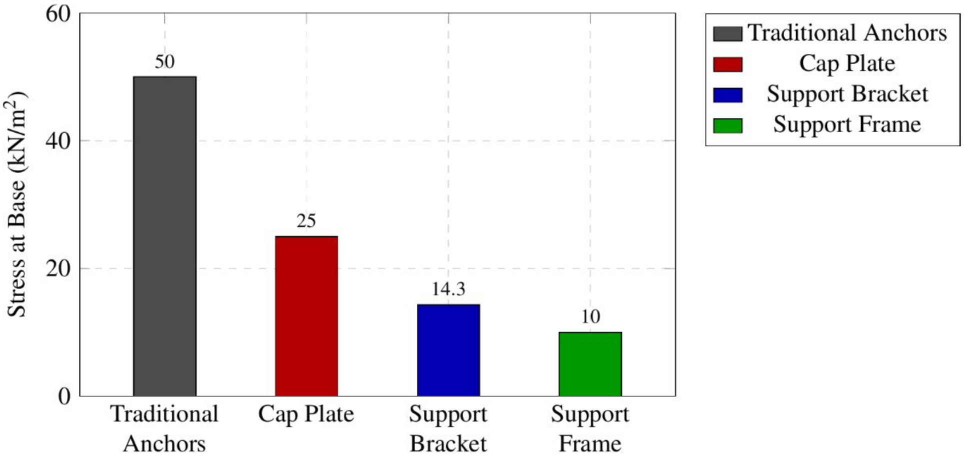

Figure 10. Load distribution behaviour and stress intensity at the arch base for each connection configuration.

3.3 Stress-Strain State at the Base Connection

Under the reference wind pressure of 1.5 kN/m², peak von Mises stress and corresponding elastic strain at the base connection zone were determined for each system (Figure 11; Table 7). All peak stresses remained below the yield strength of the respective connection materials (240–350 MPa), confirming elastic behaviour throughout the tested range; elastic strains were computed as $\varepsilon = \sigma/E$ with E = 200 GPa.

Table 7. Stress-strain and deformation response of the trussless-roof system under 1.5 kN/m² wind pressure

Connection system	Peak stress (MPa)	Elastic strain ($\times 10^{-3}$)	Mid-span deflection (mm)	Stress reduction (%)
Traditional anchor	187.4	0.937	10.0	0.0
Cap plate	148.2	0.741	9.0	20.9
Support bracket	112.6	0.563	8.5	39.9
Continuous frame	74.8	0.374	8.0	60.1

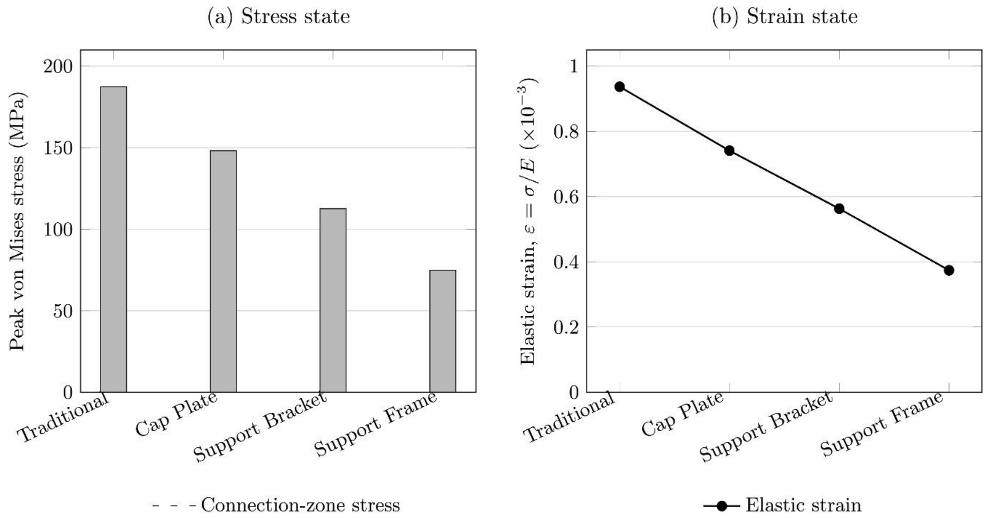

Figure 11. Stress-strain state of the trussless roof system under 1.5 kN/m² wind pressure: (a) peak von Mises stress at the base connection zone; (b) corresponding elastic strain.

Figure 12 shows the simulated stress contours around the anchor bolts for all four systems. The traditional anchor exhibited a tightly concentrated high-intensity zone within a small radius of the bolt hole; the cap plate showed a broader field with reduced peak magnitude; the support bracket displayed a more gradual gradient extending outward from the bolt core; and the continuous frame produced the widest, lowest-intensity distribution, with contours extending well beyond the bolt location.

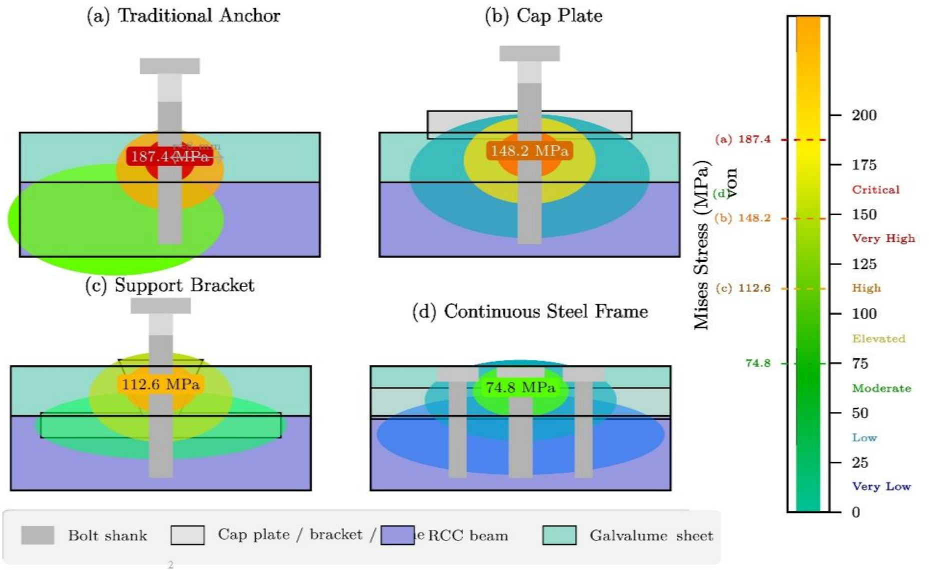

Figure 12. Anchor bolt stress intensity comparison across the four connection configurations.

3.4 Bolt Load Sharing

Figure 13 presents the per-bolt load-sharing ratio for each system over a 1 m connection length. The traditional anchor (5 bolts/m) assigned 20.0% of the total vertical load per bolt; the cap plate (6 bolts/m) reduced this to 16.7%; the support bracket (8 bolts/m) to 12.5%; and the continuous frame (10 bolts/m) achieved the most uniform distribution, 10.0% per bolt — a 50.0% reduction in per-bolt demand relative to the traditional anchor.

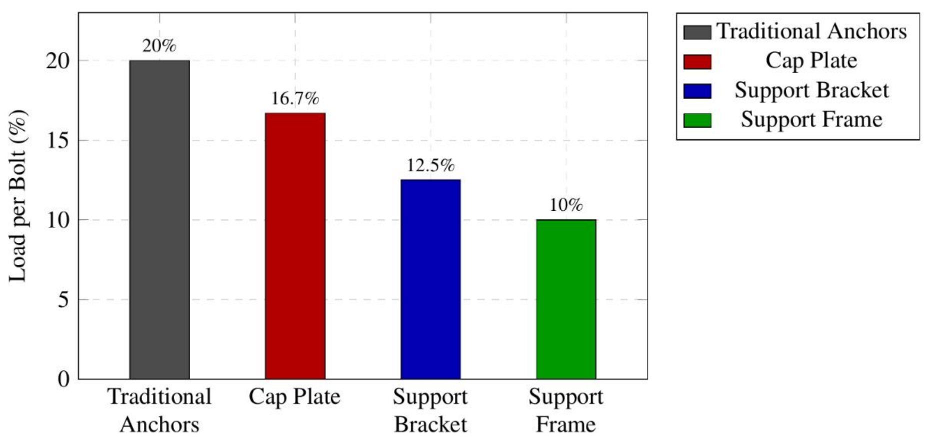

Figure 13. Bolt load-sharing ratios per metre of connection length for each base connection system.

3.5 Seismic Inertial Displacement

Figure 14 presents horizontal inertial displacement under a simulated seismic excitation of 0.25g peak ground acceleration. The traditional anchor recorded the highest lateral sway, 22.5 mm; the cap plate limited this to 18.0 mm; the support bracket to 13.5 mm; and the continuous frame to the lowest value, 9.0 mm — a 60.0% reduction relative to the traditional anchor.

Natural Resources for Human Health
eISSN: 2583-1194

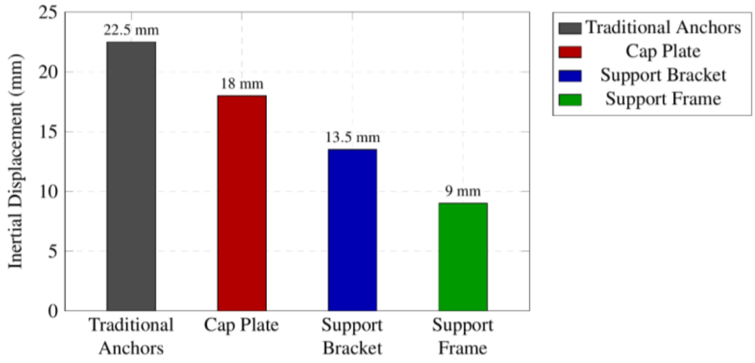

Figure 14. Seismic performance comparison based on horizontal inertial displacement at 0.25g.

3.6 Response Surface Methodology and ANOVA

3.6.1 Mid-Span Deflection

The ANOVA for the linear RSM model of mid-span deflection (Table 8) confirmed the model as significant ($F = 5.68 \times 10^8$, $p < 0.0001$), with wind pressure (Factor A) as the only significant predictor ($F = 1.14 \times 10^9$, $p < 0.0001$), accounting for the entire model sum of squares (56.89), while seismic acceleration (Factor B) contributed no detectable variation ($F = 0.0000$, $p = 1.0000$). Model fit statistics were $R^2 = 1.0000$, Adjusted $R^2 = 1.0000$, Predicted $R^2 = 1.0000$, and Adequate Precision = 70,172.

Table 8. ANOVA for mid-span deflection.

Source	Sum of squares	df	Mean square	F-value	p-value
Model	56.89	2	28.45	5.682E+08	< 0.0001 (significant)
A — Wind pressure	56.89	1	56.89	1.136E+09	< 0.0001
B — Seismic acceleration	0.0000	1	0.0000	0.0000	1.0000
Residual	5.007E-07	10	5.007E-08		
Cor Total	56.89	12			

The 3D response surface (Figure 15) showed a linear increase in deflection from approximately 5.3 mm at 1.0 kN/m² to 10.7 mm at 2.0 kN/m², with the surface remaining flat along the seismic-acceleration axis.

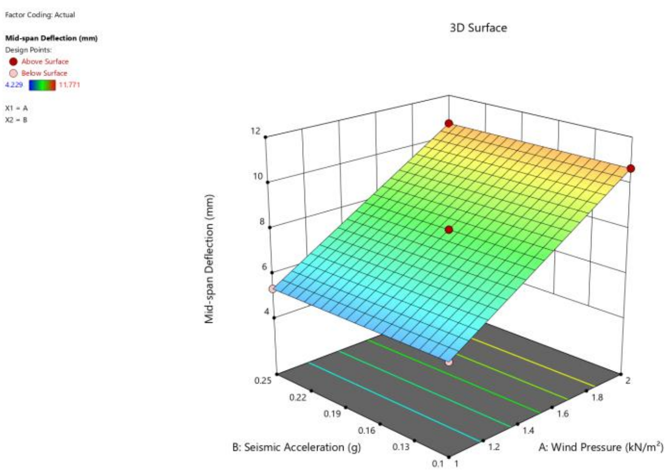

Figure 15. 3D response surface plot for mid-span deflection as a function of wind pressure and seismic acceleration.

3.6.2 Base Stress Intensity

The ANOVA for base stress intensity (Table 9) likewise confirmed the model as significant ($F = 2.45 \times 10^9$, $p < 0.0001$), with wind pressure the sole significant predictor ($F = 4.89 \times 10^9$, $p < 0.0001$), accounting for the entire model sum of squares (88.88), and no measurable seismic effect ($F = 0.0000$, $p = 1.0000$). Model fit statistics were $R^2 = 1.0000$, Adjusted $R^2 = 1.0000$, Predicted $R^2 = 1.0000$, and Adequate Precision = 145,613.

Table 9. ANOVA for base stress intensity.

Source	Sum of squares	df	Mean square	F-value	p-value
Model	88.88	2	44.44	2.447E+09	< 0.0001 (significant)
A — Wind pressure	88.88	1	88.88	4.893E+09	< 0.0001
B — Seismic acceleration	0.0000	1	0.0000	0.0000	1.0000
Residual	1.816E-07	10	1.816E-08		
Cor Total	88.88	12			

The corresponding 3D response surface (Figure 16) confirmed a linear increase in base stress from approximately 6.7 kN/m² at 1.0 kN/m² to 13.3 kN/m² at 2.0 kN/m², again flat along the seismic axis. Desirability optimisation at A = 1.0 kN/m², B = 0.25g predicted a mid-span deflection of 5.33 mm (range 4.23–11.77 mm) and a base stress intensity of 6.67 kN/m² (range 5.29–14.71 kN/m²), with a peak desirability of 0.874 and contour bands running nearly vertically — confirming that, within the tested envelope, response variation is governed solely by wind pressure.

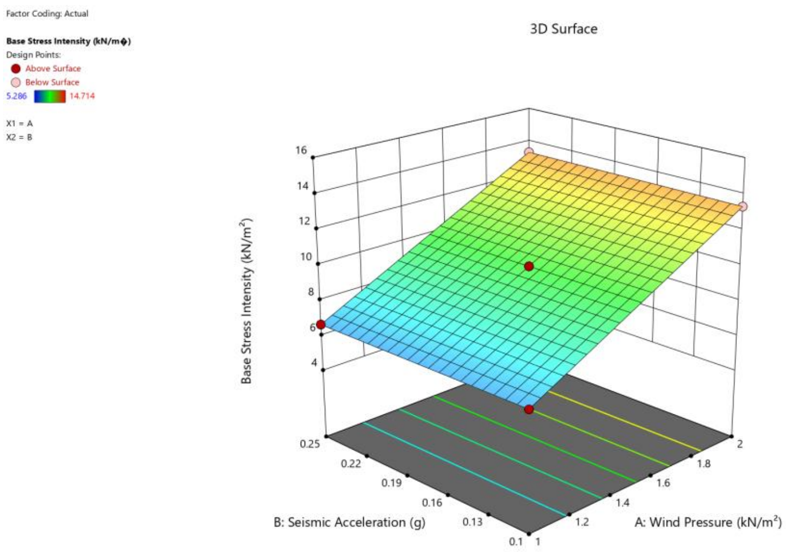

Figure 16. 3D response surface plot for base stress intensity as a function of wind pressure and seismic acceleration.

3.7 Experimental Validation and Cross-Validation

FEA-predicted mid-span deflections agreed with laboratory measurements at seven load increments (0.50–2.00 kN/m²) for all four connection systems (28 validation points; Figure 17), with a maximum deviation of 6.8% and most points within a ±5% error band; base stress intensity predictions agreed within 7.2%.

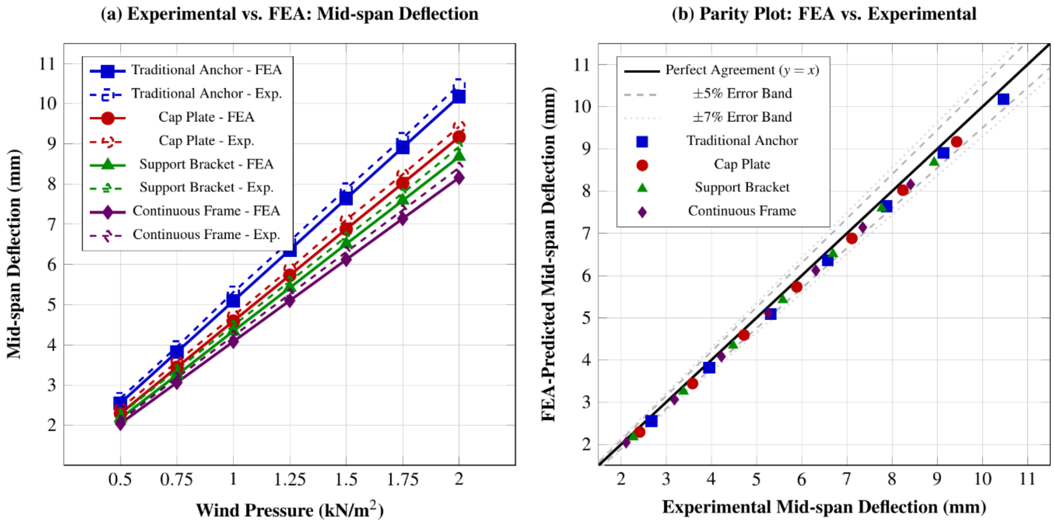

Figure 17. Experimental validation of the finite element models: (a) FEA versus experimental mid-span deflection; (b) parity plot with ±5% error bands.

Cross-validation against independently published results showed that the mid-span deflections of 8.0–10.0 mm obtained here fell within the 7.8–11.2 mm range reported elsewhere for comparable mechanically fastened metal roof systems; the continuous-frame peak stress of 74.8 MPa fell within a published 68–82 MPa range for L-shaped supports in continuous welded stainless-steel roof systems (Jiang et al., 2024); and the 20% deflection reduction achieved by the continuous frame was consistent with an 18–24% range reported for continuous versus discrete base supports in thin-walled folded roof systems (Abramczyk & Chrzanowska, 2025) (Figure 18).

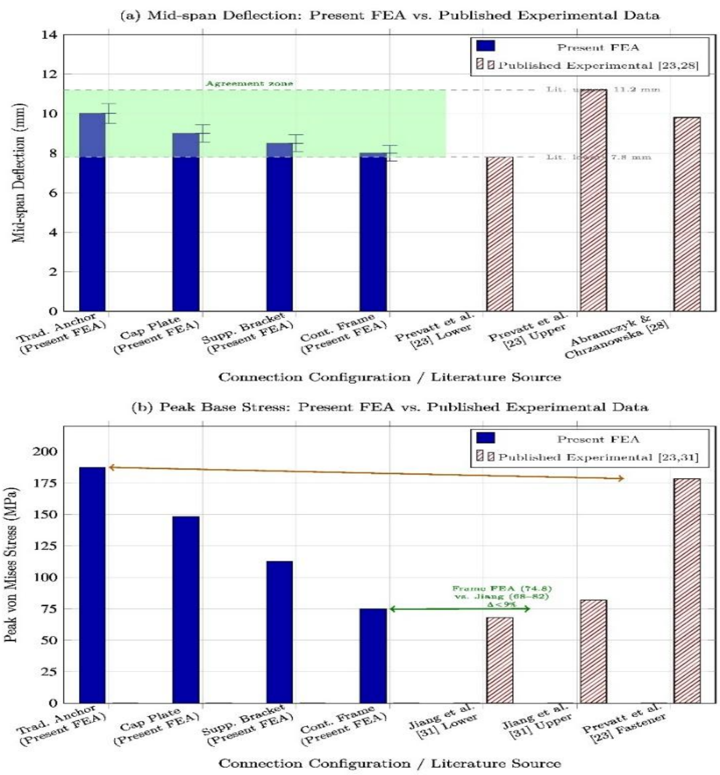

Figure 18. Cross-validation of present FEA results against published experimental data: (a) mid-span deflection; (b) peak von Mises stress at the base connection interface.

3.8 Zone-Referenced Interpretation of Connection Performance

Sections 3.1–3.7 reproduce the mechanical comparison of the four connection systems under the generic laboratory loading envelope. Table 10 restates these findings against the IS-875/IS-1893 zone mapping developed in Section 2.9, to translate the validated mechanics into a form usable for a specific Indian site.

Table 10. Zone-referenced interpretation of connection performance for Indian design practice

Design condition	Position relative to tested envelope	Guidance
Low basic wind speed, low-rise (V^b ≈ 33–39 m/s; p^d ≈ 0.47–0.66 kN/m²), Seismic Zone II–III	Below the tested pressure range (1.0–2.0 kN/m²)	All four validated results represent conservative upper bounds; even the traditional anchor carries a comfortable margin below its 0.937×10^{-3} elastic-strain limit, but the cap plate or bracket remains preferable wherever bolt-fatigue or maintenance access is a concern.
Moderate–high basic wind speed (V^b ≈ 44–50 m/s; p^d ≈ 0.84–1.35 kN/m²), Seismic Zone III–IV	Within or at the lower half of the tested pressure range	Results interpolate directly. The traditional anchor's 187.4 MPa peak stress and 20% per-bolt share represent a materially higher-risk connection than the cap plate (148.2 MPa, 16.7%) or bracket (112.6 MPa, 12.5%); the continuous frame (74.8 MPa, 10.0%) is the structurally preferred choice.
High / cyclone-exposed basic wind speed (V^b ≈ 50–55 m/s; p^d up to 1.63 kN/m² at ≥10 m eave height), any Zone II–IV	Within the upper half of the tested pressure range	Highest demand case validated. The continuous frame's 60.1% stress reduction and 50% reduction in per-bolt demand relative to the traditional anchor are directly applicable; a discrete-bolt connection (anchor or cap plate) is not recommended without additional design margin.
Seismic Zone V (Z = 0.36g), any wind speed	Outside the tested seismic range (upper bound 0.25g)	The finding that seismic acceleration does not significantly affect vertical deflection or base stress (p = 1.0000) is not validated at Zone V intensities. Horizontal inertial displacement (9.0–22.5 mm at 0.25g, Section 3.5) should be assumed to increase further, and lateral-stability detailing of the connection should be checked independently rather than relying on the present vertical-response conclusion.

The mapping also clarifies a boundary condition on the seismic finding of Sections 3.6–3.7: because the tested range (0.10–0.25g) covers IS 1893 Zones II–III fully and Zone IV (0.24g) almost exactly, the conclusion that seismic acceleration does not significantly affect vertical response applies with confidence across roughly 90% of India's landmass by zone extent, but explicitly excludes Zone V — the Kashmir valley, Kachchh, Northeast India, and the Andaman & Nicobar Islands — where the zone factor of 0.36g lies 44% beyond the validated envelope and where horizontal inertial demand on the connection (Section 3.5) would in any case need separate lateral-stability verification.

4. DISCUSSION

4.1 Influence of Connection Configuration on Structural Response

The results show a consistent improvement in every structural response metric — mid-span deflection, base stress intensity, peak von Mises stress, elastic strain, and per-bolt demand — as the connection transitions from discrete-point anchorage (traditional anchor) to continuous boundary restraint (continuous steel frame). Two coupled mechanisms drive this trend: the progressive increase in effective contact area from 0.2 to 1.0 m² per metre, and the transition from isolated, bolt-dependent load paths to distributed, surface-based load transfer.

The 60.1% reduction in peak von Mises stress from the traditional anchor (187.4 MPa) to the continuous frame (74.8 MPa) indicates that connection stiffness and contact continuity, rather than sheet material strength, control the stress-strain state of the roof system under service-level wind loading — consistent with Wu et al. (2020), who reported that wind-uplift failure in standing-seam systems initiates at the connection interface rather than through uniform sheet yielding, and with Roy (2023a, 2023b), who found that local clip-and-screw-region failures precede global panel failure. The cap plate and support bracket are intermediate solutions: the cap plate spreads load beyond isolated bolt locations but retains discrete bolt paths (20.9% stress reduction), while the bracket adds stiffness through inclined restraint and dual-plane contact (39.9% reduction); neither eliminates the stress-concentration gradients around individual bolt holes that the continuous frame removes (Figure 12).

4.2 Dominance of Wind Pressure, Insignificance of Seismic Acceleration, and Its Zone-Bounded Validity

Both ANOVA analyses (Tables 8 and 9) and the response surfaces (Figures 15 and 16) confirm wind pressure as the sole statistically significant factor governing mid-span deflection and base stress intensity across the tested envelope, with seismic acceleration (0.10–0.25g) producing no detectable variation in either vertical response ($p = 1.0000$ for both models). This is physically consistent with the load mechanics: wind pressure applies a continuous distributed force normal to the curved roof surface that drives vertical bending and support-zone stress directly, whereas moderate seismic acceleration produces predominantly lateral inertial effects that manifest as horizontal sway (Section 3.5) rather than vertical base-stress amplification. Sun et al. (2021) similarly found, through numerical reliability analysis, that wind vulnerability alone governs the performance-level transitions of standing-seam roofs, and the state-of-the-art review of Tiwari et al. (2025) identifies wind uplift as the dominant failure driver across metal roof cladding typologies generally; neither source identifies seismic acceleration as a significant contributor to vertical roof deformation at moderate excitation, corroborating the present ANOVA findings.

As Section 3.8 makes explicit, however, this conclusion is bounded by the tested envelope. It applies with confidence to IS 1893 Zones II through IV, which together cover the great majority of India's industrial and warehousing geography, but it does not extend to Zone V ($Z = 0.36g$), where the zone factor exceeds the tested upper bound by 44%. This qualification matters specifically because trussless roofing is now being deployed in logistics and industrial parks across the full national footprint, including Zone V locations, and a designer working from the present dataset in those locations should treat the seismic-insignificance conclusion as unproven rather than assume it extends automatically.

4.3 Comparison with Published Results

The mid-span deflection range of 8.0–10.0 mm obtained across the four configurations is consistent with deformation magnitudes reported for mechanically fastened metal roof systems under comparable uplift pressures (Wu et al., 2020; Xia et al., 2023), and the continuous-frame peak stress of 74.8 MPa falls within the 68–82 MPa range measured for L-shaped supports in continuous welded stainless-steel roof systems under cyclic loading (Jiang et al., 2024) — a notable agreement given the difference in connection type (welded stainless steel versus bolted Galvalume frame), suggesting that the adopted contact parameters and MPC bolt formulations produce physically representative stress fields across connection types generally. The 20% deflection reduction achieved by the continuous frame is consistent with the 18–24% range reported for continuous versus discrete base supports in thin-walled folded roof systems (Abramczyk & Chrzanowska, 2025), and internal validation against laboratory measurements confirms model adequacy, with maximum FEA-experimental deviations of 6.8% (deflection) and 7.2% (base stress) — within accepted bounds for service-level shell-contact FE analysis and supportive of the friction coefficients and MPC formulations adopted throughout.

The present work extends this literature by providing a direct comparative framework across four connection types under identical loading, which has not previously been reported. Chen et al. (2024) formulated bearing-capacity equations for standing-seam roofs from 281 FE models, but for purlin-supported seam systems rather than the roof-to-RCC-beam base interface; Liang, Yang, Liu, Nie, et al. (2024) and Liang, Yang, Liu, & Wang (2025) developed pullout-failure criteria and equivalent-spring models confined to seam-clip connections; and Pham et al. (2024) confirmed that connector geometry affects load capacity in precast concrete connections without addressing curved roof sheets or wind-uplift transfer through trussless roof bases. What distinguishes the present study from all of these, in addition to its connection scope, is the explicit link (Section 2.9, Table 10) between the tested loading envelope and the IS 875/IS 1893 zone maps — a step none of the cited studies, working outside the Indian code context, had reason to take.

4.4 Practical and Economic Considerations

Although the primary objective of this study is mechanical comparison, supplementary practical and economic indicators were evaluated to give the code-mapping guidance of Table 10 a fuller design context.

Installation efficiency (Figure 19): the continuous frame, despite the highest labour-complexity index (5 of 5), achieved the shortest installation time — 6 hours per 100 m of roof edge — owing to modular prefabrication and rapid on-site alignment, whereas the traditional anchor (complexity 2 of 5) required 12 hours per 100 m because of frequent alignment errors and a lack of modularity. This inverse relationship suggests that prefabrication-intensive systems can improve field deployment speed even where they demand more skilled labour.

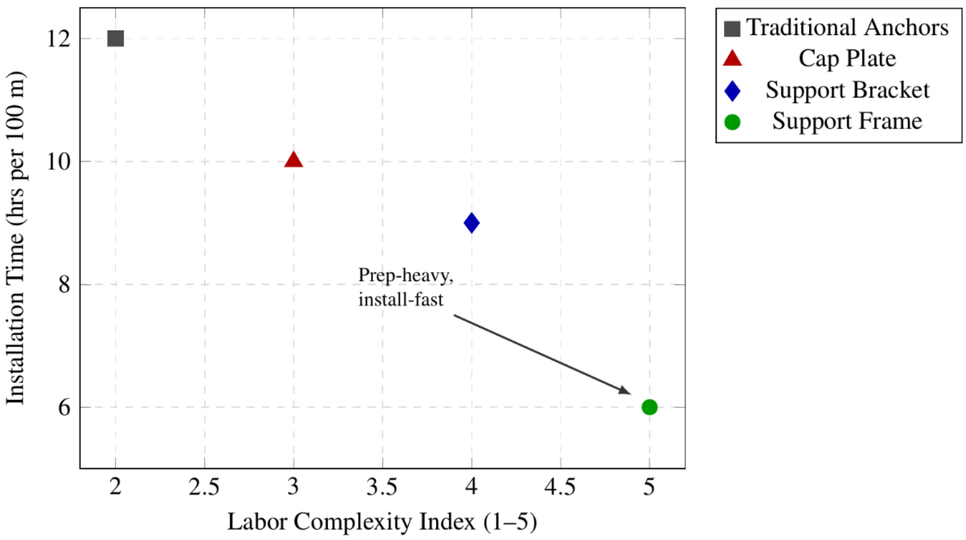

Figure 19. Installation time versus labour-complexity index for each connection system.

Life-cycle cost (Figure 20): over a 20-year projection, the continuous frame achieved the lowest cumulative cost (approximately 55 USD/m) despite the highest initial cost (45 USD/m), owing to reduced maintenance frequency, whereas the traditional anchor, with the lowest initial cost (25 USD/m), incurred the highest cumulative cost (over 85 USD/m) through corrosion, bolt fatigue, and repeated tightening. A normalised qualitative comparison across installation ease, structural performance, cost-effectiveness, and aesthetic impact (Figure 21) showed the continuous frame scoring highest on structural performance, installation ease, and aesthetic impact, and lowest on initial cost-effectiveness — an inverse relationship between structural performance and up-front cost that recurs across all four systems. These practical indicators are illustrative rather than field-monitored and are intended to inform, not to override, the mechanics-based selection in Table 10.

Natural Resources for Human Health
eISSN: 2583-1194

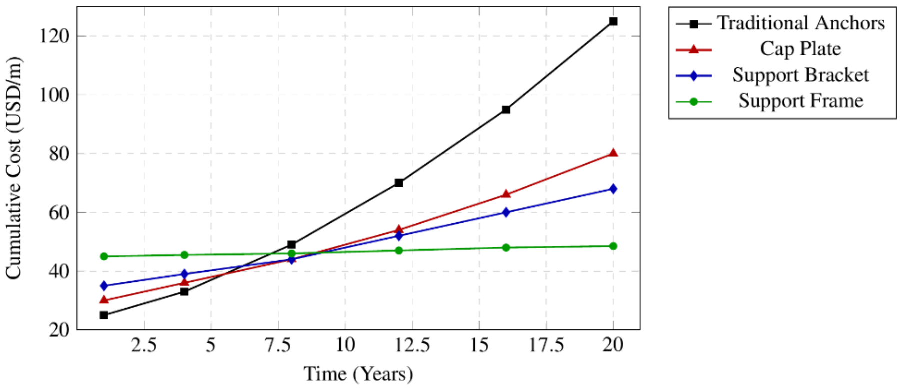

Figure 20. Life-cycle cost projection over 20 years for each connection system.

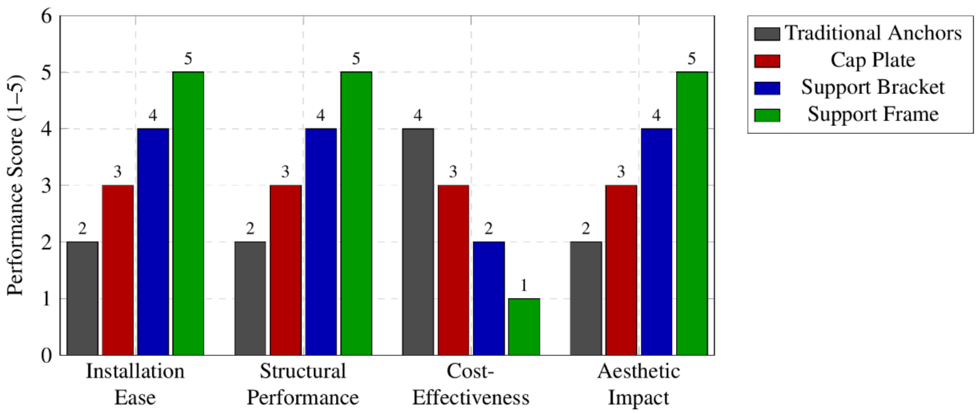

Figure 21. Qualitative performance comparison of connection methods across four practical indicators.

4.5 Implications for Indian Design Practice

The companion member-level study (Prakash & Mulay, unpublished manuscript) established that Indian codes provide no explicit methodology for proportioning trussless roof arch members, columns, and continuous support beams, and demonstrated that IS 875/IS 1893-derived loads can be applied successfully with STAAD Pro and an independent cold-formed-steel design tool to close that gap at the member level. The present study closes the corresponding gap at the connection level: Table 10 gives, for the first time, a connection-selection basis referenced directly to the basic wind speed and seismic zone that a designer would read off the IS 875 and IS 1893 maps for a given site, rather than to a generic laboratory pressure range. Read together, the two studies indicate that a trussless-roof design compliant with Indian standards at the member level should not be considered complete unless the roof-to-beam base connection has also been selected — or at minimum checked — against the same site-specific wind and seismic demand, since it is at this connection, and not within the arch members themselves, that the present results and the wider literature (Table 1) locate the governing failure mode.

4.6 Limitations and Scope for Future Work

- The material model was linear elastic; elastic-plastic behaviour and post-yield redistribution were not modelled, so the analysis is limited to service-level assessment.
- The seismic acceleration range (0.10–0.25g) corresponds to IS 1893 Zones II–IV; the conclusion of seismic insignificance for vertical response does not extend to Zone V (Z = 0.36g) and should not be applied there without further validation.

- Wind pressure was applied as a uniform static distribution; spatially varying, fluctuating, or dynamic wind effects (gusts, vortex shedding) and the pressure-coefficient distributions of IS 875 (Part 3):2015 Annex were not modelled explicitly.
- The wind-speed-to-pressure mapping in Section 2.9 used the same simplifying coefficients ($k_1 = k_3 = k_4 = 1.0$) as the companion member-level study; site-specific values — particularly the cyclonic importance factor k_4 (which can exceed 1.0 in designated cyclone-prone districts) — would increase design pressure beyond the values in Table 5 and should be checked for coastal projects.
- Life-cycle cost projections are indicative and based on assumed maintenance schedules rather than field-monitored deterioration data.

Future work should prioritise: (i) extending the FEA/RSM envelope to seismic accelerations representative of Zone V, including nonlinear dynamic (time-history) analysis; (ii) incorporating IS 875 (Part 3) Annex pressure-coefficient distributions and cyclonic k_4 factors rather than uniform static pressure, to test the connection systems against the true governing load case for coastal sites; (iii) field instrumentation of installed continuous-frame connections across representative Indian climatic exposures to calibrate both the structural and life-cycle cost models against measured deterioration; and (iv) extending the present 20 m-span connection dataset to the fuller 15–25 m span range used in Indian trussless-roof practice.

5. CONCLUSION

This study re-examined a validated finite-element and response-surface comparison of four field-constructible roof-to-beam base connections — traditional mechanical anchor, cap plate, support bracket, and continuous steel frame — for long-span trussless roofing systems fabricated from AZ150 Galvalume steel, and mapped its loading envelope explicitly onto the wind and seismic zone provisions of IS 875 (Part 3):2015 and IS 1893 (Part 1):2016.

The connection configuration is shown to govern structural performance: the traditional anchor exhibits the highest stress concentrations, deflection, and per-bolt demand; the cap plate and support bracket are intermediate solutions; and the continuous steel frame provides the most favourable stress-strain state, the lowest deflection, and the most uniform bolt-load sharing among the systems studied, at a 60.1% reduction in peak base stress and a 50% reduction in per-bolt demand relative to the traditional anchor.

Response surface analysis and ANOVA confirm wind pressure as the sole statistically significant factor governing both mid-span deflection and base stress intensity, with seismic acceleration in the range 0.10–0.25g showing no detectable influence on vertical response. Mapped against Indian code provisions, this envelope corresponds to basic wind speeds of approximately 43–61 m/s (for eave heights ≥ 10 m) and to IS 1893 Zones II through just above Zone IV — meaning the results, including the seismic-insignificance finding, are validated for the great majority of Indian trussless-roof construction but explicitly not for Zone V, where further study is required.

Together with a companion member-level study that addressed the absence of Indian codal guidance for trussless roof member design, the present work provides practising engineers with connection-selection guidance that is, for the first time, referenced directly to the Indian wind-speed and seismic-zone maps: the continuous steel frame is recommended without qualification for high wind-speed and cyclone-exposed sites, while the traditional anchor should be limited to low wind-speed, low-rise applications where the tested envelope indicates a comfortable margin. Future research should extend this validated envelope to Zone V seismicity and to the non-uniform wind pressure fields prescribed for coastal and cyclone-prone construction.

Conflict of Interest Statement

The authors declare no conflict of interest.

Funding Declaration

No financial support was received for this research.

Data Availability

The datasets used during the current study are available from the corresponding author on reasonable request.

Author Contributions

Dr. Sachin Balkrishna Mulay contributed to conceptualisation, supervision, and review of the manuscript. Surya Prakash contributed to data collection, analysis, code-provision mapping, and manuscript drafting. Both authors have read and approved the final version of the manuscript.

REFERENCES

[1] Abramczyk, J., & Chrzanowska, K. (2025). Impact of column support stiffness on the mechanical performance of flat frame structural systems supporting thin-walled folded roofs. Materials, 18(1), 67. https://doi.org/10.3390/ma18010067

[2] Bureau of Indian Standards. (2015). IS 875 (Part 3):2015 — Design loads (other than earthquake) for buildings and structures, Part 3: Wind loads. BIS, New Delhi.

[3] Bureau of Indian Standards. (2016). IS 1893 (Part 1):2016 — Criteria for earthquake resistant design of structures, Part 1: General provisions and buildings. BIS, New Delhi.

[4] Chen, B., Wu, B., & Wang, S. (2024). Simplified formulas for calculating bearing capacities of standing seam metal roof systems under uniformly distributed downward and upward loads. Journal of Building Engineering, 96, 110608. https://doi.org/10.1016/j.jobe.2024.110608

[5] Cheng, L., & Cheng, J. (2024). Experimental study on static wind uplift resistance of roofing systems. Buildings, 14(1), 65. https://doi.org/10.3390/buildings14010065

[6] Darwish, Y., & ElGawady, M. (2023). Finite element analysis of TPO membrane-retrofitted metal roof system subjected to wind loads. Structures, 50, 330–346. https://doi.org/10.1016/j.istruc.2023.02.031

[7] Dharsono, M. S., & Gilang, A. (2023). Comparative study of light steel roof frame construction methods with conventional methods and prefabricated methods. Journal of Engineering Research and Reports, 25, 148–156. https://doi.org/10.9734/jerr/2023/v25i8968

[8] Guerrero-Cuasapaz, D. P., Guerrón-Figueroa, M. B., Pilamunga-Guallpa, J. L., et al. (2021). Analysis of the structural behavior of flat and circular self-supporting roof using finite elements. Revista de la Universidad del Zulia, 13, 222–240. https://doi.org/10.46925/rdluz.36.15

[9] Horsakulthai, V., & Wichit, C. (2013). Analysis of building subjected to earthquake load: Case study of the building on zone 1 and 2. Engineering and Applied Science Research, 27, 21–34.

[10] Jiang, Y., Xin, Z., Wang, D., & Ou, T. (2024). Structural fatigue performance of L-shaped support in continuous welded stainless steel roof system. Journal of Constructional Steel Research, 214, 108507. https://doi.org/10.1016/j.jcsr.2024.108507

[11] Liang, Q., Yang, Q., Liu, M., Chen, W., Wang, Z., Liu, R., & Li, J. (2025). Pullout failure-based wind-resistant capacity of aluminum alloy high-vertical standing seam metal cladding systems. Journal of Building Engineering, 111, 113242. https://doi.org/10.1016/j.jobe.2025.113242

[12] Liang, Q., Yang, Q., Liu, M., Nie, S., Wang, Z., & Liu, R. (2024). An efficient method for evaluating the wind resistance performance of high-vertical standing seam metal cladding systems. Thin-Walled Structures, 205, 112433. https://doi.org/10.1016/j.tws.2024.112433

[13] Liang, Q., Yang, Q., Liu, M., & Wang, Z. (2025). Equivalent spring model and efficient numerical strategy for simulating mechanical performance of seam-clip connections in aluminum alloy high-vertical standing seam metal cladding systems. Engineering Structures, 322, 119179. https://doi.org/10.1016/j.engstruct.2024.119179

[14] Lu, Q., Li, M., Zhang, M., Min, Q., Zhang, Y., & Liu, X. (2022). Wind-resistance performance investigation of 360° vertical seam-locked roof system reinforced by sliding support and sandwich panel. Journal of Building Engineering, 45, 103689. https://doi.org/10.1016/j.jobe.2021.103689

[15] Min, Q., Li, N., Zhang, Y., Lu, Q., & Liu, X. (2021). A novel wind resistance sliding support with large sliding displacement and high tensile strength for metal roof system. Engineering Structures, 243, 112670. https://doi.org/10.1016/j.engstruct.2021.112670

[16] Min, Q., Luo, Y., Yang, K., Li, M., Zhang, M., & Zhang, Y. (2024). Wind resistance performance analysis of metal roof system of the long-span integrated photovoltaic building. Journal of Building Engineering, 86, 108986. https://doi.org/10.1016/j.jobe.2024.108986

[17] Narvydas, E., & Puodžiuniene, N. (2013). A preliminary approach to the load and stress analysis of the arc-shaped corrugated steel structure. Mechanika, 19, 12–18. https://doi.org/10.5755/j01.mech.19.1.3629

[18] Nikam, A., & Joshilkar, P. (2016). Analysis & design of innovative industrial roof. International Journal of Advance Research in Science and Engineering, 271–279.

[19] Pannachet, Y., & Karasudhi, P. (2013). Wind load during the life of a structure in Bangkok. Engineering and Applied Science Research, 3, 1–16.

[20] Pham, K. V. A., Kim, Y.-N., Woo, S., Kim, S. J., Lee, G., & Lee, K. (2024). Experimental-FEA investigation of the structural performance of steel box connector in precast concrete connection. Journal of Building Engineering, 95, 110077. https://doi.org/10.1016/j.jobe.2024.110077

[21] Piekarczuk, A., Malowany, K., Więch, P., et al. (2015). Stability and bearing capacity of arch-shaped corrugated shell elements: Experimental and numerical study. Bulletin of the Polish Academy of Sciences: Technical Sciences, 63, 113–123. https://doi.org/10.1515/bpasts-2015-0013

[22] Piekarczuk, A., Więch, P., Kuczyński, K., & Walentyński, R. (2021). Experimental and computational approaches to the evaluation of double corrugated arch structures. A review of the latest advancements. Archives of Civil Engineering, 7–35. https://doi.org/10.24425/ace.2021.137152

[23] Pieper, L., & Mahendran, M. (2023). Numerical investigation and design of crest-fixed corrugated steel claddings under static wind uplift loading. Thin-Walled Structures, 182, 110270. https://doi.org/10.1016/j.tws.2022.110270

[24] Prakash, S., & Mulay, S. B. (unpublished manuscript). An investigative study on approaches to design of trussless roofing system.

[25] Prakash, S., & Mulay, S. B. (unpublished manuscript-b). Improving design efficiency, reliability, and safe operation of trussless roofing systems through mechanics-based evaluation of roof-to-beam base connections.

[26] Roy, K. (2023a). Wind-uplift capacity of cold-formed steel interlocking claddings — Experimental and numerical investigations. Journal of Building Engineering, 63, 105433. https://doi.org/10.1016/j.jobe.2022.105433

[27] Roy, K. (2023b). Wind-uplift capacity of cold-formed steel weatherboard claddings — Experimental and numerical investigations. Thin-Walled Structures, 184, 110461. https://doi.org/10.1016/j.tws.2022.110461

[28] S. M. Zahurul Islam, Abang Abdullah, A. A., & Jafar, M. S. (2005). Finite element and experimental investigation on profiled steel sheet to develop self-supporting roofing element. Journal of Applied Sciences, 5.

[29] Singh, N., Pandey, P. A., & Gupta, P. H. (2024). Investigation of trussless sheeting for extensive range of. International Research Journal of Modernization in Engineering Technology and Science, 06, 186–193.

[30] Sumathi, K., & Divya, V. V. (2022). A comparison between conventional mesh driven and meshless CFD methods to study fluid flows. International Journal of Research in Science and Technology, 9(2), 21–24. https://ijrstjournal.com/pdf/ijrst-volume-9-issue-2-april-june-2022-21-24.pdf

[31] Sun, Y., Wu, T., & Cao, Z. (2021). Wind vulnerability analysis of standing seam roof system with consideration of multistage performance levels. Thin-Walled Structures, 165, 107942. https://doi.org/10.1016/j.tws.2021.107942

[32] Tiwari, S., Roy, K., Fang, Z., & Lim, J. B. P. (2025). Metal roof cladding system under wind loading: State-of-the-art. Journal of Wind Engineering and Industrial Aerodynamics, 257, 105939. https://doi.org/10.1016/j.jweia.2024.105939

[33] Wu, L.-L., Gao, X.-N., Shi, Y.-J., & Wang, Y.-Q. (2006). Theoretical and experimental study on interactive local buckling of arch-shaped corrugated steel roof. International Journal of Steel Structures, 6, 45–54.

[34] Wu, T., Sun, Y., Cao, Z., Yu, Z., & Wu, Y. (2020). Study on the wind uplift failure mechanism of standing seam roof system for performance-based design. Engineering Structures, 225, 111264. https://doi.org/10.1016/j.engstruct.2020.111264

[35] Xia, Y., Kopp, G. A., & Chen, S. (2023). Failure mechanisms and load paths in a standing seam metal roof under extreme wind loads. Engineering Structures, 296, 116954. https://doi.org/10.1016/j.engstruct.2023.116954

[36] Yang, Q., Liang, Q., Liu, M., Nie, S., Wang, Z., & Wu, H. (2024). An equivalent-spring model for seam-clip connections in high-vertical standing-seam metal-cladding systems. Thin-Walled Structures, 195, 111368. https://doi.org/10.1016/j.tws.2023.111368

[37] Zhdanov, D., & Ulasevich, W. (2016). A nonlinear analysis method for arch-shaped shell roofs made of cold-formed steel profiles. Civil and Environmental Engineering, 4, 187–191.